Finite-Wing and Sweep Effects on Transonic Buffet Behavior

D'Aguanno, A.; Schrijer, F.F.J.; van Oudheusden, B.W.

DOI
10.2514/1.J061974

Publication date
2022

Document Version
Final published version

Published in
AIAA Journal: devoted to aerospace research and development

AIAA JOURNAL
Vol. 60, No. 12, December 2022

Finite-Wing and Sweep Effects on Transonic Buffet Behavior

Alessandro D'Aguanno,* Ferdinand F. J. Schrijer,† and Bas W. van Oudheusden‡
Delft University of Technology, 2629 HS Delft, The Netherlands

https://doi.org/10.2514/1.J061974

This study experimentally investigates the effects of the sweep angle and finite wing on transonic buffet, studying two-dimensional (2-D) and three-dimensional wing configurations. Background-oriented schlieren and stereographic particle image velocimetry (PIV) have been used as measurement techniques, performing experiments on an OAT15A airfoil (clamped to both the side windows of the wind tunnel), an unswept wing, and two swept wings with sweep angles of 15 and 30 deg, respectively. The three wings are also based on the OAT15A airfoil and are clamped at the wind tunnel only at their root (free wingtip). All wings have been tested at a constant normal Mach number ($Ma_{\infty n} = 0.7$) with respect to the leading edge. The results show that the buffet oscillations are much stronger for the airfoil than for the three finite-span wings. A large difference in the buffet behavior can be noticed between the airfoil and the unswept wing, as is also seen in oil flow visualizations. This difference is particularly evident in correspondence of the more outboard spanwise locations, suggesting that for the unswept wing, an important role could be played by finite-wing effects: notably, the tip vortex. A spectral analysis has shown that for the swept wings, the classical 2-D buffet peak (occurring at $f = 160$ Hz for the present conditions) is substantially attenuated, whereas additional contributions in the range of 450–850 Hz appear. The PIV results showed, for the 30 deg sweep angle wing, a periodical occurrence of a secondary supersonic area downstream of the main shock wave structure, which is absent for the other wing models. The stereographic PIV configuration allowed the reconstruction of the spanwise-oriented velocity component, obtaining, in proximity of the trailing-edge, values of the spanwise velocity component (80–100 m/s) which are in agreement with the spanwise convection of buffet cells observed in the literature in this region.

I. Introduction

THE flight envelope of civil aircraft is limited by the onset of transonic buffet. This phenomenon consists of the oscillation of a shock wave on the suction side of the wing, which occurs for a specific range of angle of attack α, Mach number Ma, and Reynolds number Re. These oscillations could eventually result in failure of the wing due to fatigue as well as to unsteadiness in the aerodynamic characteristics.

The occurrence of transonic wing buffet has been extensively studied in the last 30 years, notwithstanding that the first studies had already been undertaken as early as 1947 in Ref. [1]. This phenomenon was explained in 1990 in Ref. [2] as the result of a feedback mechanism, with the shock wave (SW) oscillation being sustained by the presence of downstream-propagating vortical structures, which travel from the shock foot toward the trailing-edge area, and by upstream-traveling pressure waves [i.e., upstream-traveling pressure waves (UTWs) (induced by the presence of the vortical structures) that], moving in the direction of the shock wave (according to the buffet phase), allow the SW to move either downstream or upstream.

This physical model has been subsequently updated by different researchers, such as the authors of Refs. [3,4], who considered the UTWs capable of reaching the SW along both the suction and the pressure sides of the airfoil. Recently, a dedicated study undertaken in Ref. [5] clarified that the UTWs are acoustic waves that propagate with a velocity of 80 m/s relative to the flow. A further investigation of Ref. [6] has given hints that the UTWs are produced during the entire buffet cycle, albeit with a modulated strength depending on the buffet cycle phase.

A crucial contribution to the understanding of transonic two-dimensional (2-D) buffet has been given by the authors of Ref. [7], who described transonic buffet as the result of a modal instability, obtaining values for the buffet onset conditions that are in perfect agreement with experimental observations. These results were also validated by the stability analysis of Ref. [8].

All the previous studies were conducted on airfoils corresponding to unswept infinite-wing conditions, whereas more dedicated research on swept wings has been pursued only in more recent years. The study of buffet on swept wings is very relevant because of its possible occurrence in real flight conditions and actual wing configurations; however, a complete comprehension of the phenomenon is still far from being achieved. In the presence of wing sweep, the buffet mechanism appears to be much more complicated, with oscillations of the shock wave in the chordwise direction being of lower amplitude [9] as compared to the airfoil case and occurring at much higher frequencies. For swept wings, the typical 2-D isolated peak at $St = 0.07$ is substituted by a broadband peak in the range of $0.2 < St < 0.6$, with St being the Strouhal number based on the freestream velocity and the chord of the wing ($St = f \cdot c/U_\infty$). From the recent experiments in Ref. [10] on a 30 deg swept wing based on the OAT15A airfoil, a buffet onset of $Ma = 0.82$ at $\alpha = 3$ deg was obtained. It should be noticed that the angle of attack has an important influence as well, inducing either simultaneous 2-D and three-dimensional (3-D) shock-buffet behaviors or only 3-D behavior, depending on the trailing-edge separation characteristics [11]. The simultaneous presence of these two behaviors is also confirmed by a modal decomposition (of a zonal detached-eddy simulation) on a wing/body configuration [12].

Reference [13] described the flow pattern of a 30 deg swept wing based on the OAT15A airfoil section, resulting in a normal shock wave and a quasi-2-D flow for outboard locations, as well as a λ shock and highly 3-D flow for inboard locations.

Reference [14] studied the effect of the sweep angle, obtaining that for infinite wings with sweep angles larger than 20 deg, the difference in behavior with respect to 2-D models is very relevant. In contrast, for sweep angles of $\Lambda < 20$ deg, no substantial difference is observed. The main cause for this difference is associated with the spanwise convection of particular flow structures that occurs at high sweep angles, which was referred to in Ref. [14] as buffet cells. The buffet cells consist of pressure disturbances of alternating signs,

Presented as Paper 2022-1807 at the AIAA SciTech 2022 Forum, San Diego, CA, January 3–7, 2022; received 19 April 2022; revision received 29 July 2022; accepted for publication 27 August 2022; published online 30 September 2022.

*Ph.D. Candidate, Aerodynamics Section (Department of Flow Physics and Technology); A.Daguanno@tudelft.nl (Corresponding Author).

†Assistant Professor and Scientific Director of the Department of Flow Physics and Technology Laboratory, Aerodynamics Section (Department of Flow Physics and Technology).

‡Associate Professor, Aerodynamics Section (Department of Flow Physics and Technology).

which are periodically convected from the wing root (aft of the λ shock) toward the wingtip.

The presence of buffet cells is also confirmed by different experimental studies such as in Refs. [9–11]. In Ref. [9], different experimental databases belonging to four projects (BUFET'N Co, AVERT, DTP tremblement, and FLIRET) are compared. The different datasets were all based on wings with a sweep angle of 30 deg, and they all showed the presence of a spanwise convection velocity equal to $0.25 \cdot U_\infty$ proceeding outboard in the shock wave oscillation range. In addition to the previous convection phenomenon, another spanwise convection velocity of 100 m/s ($0.36 \cdot U_\infty$) was observed in the separated area, with similar results also obtained in Ref. [15]. Convection phenomena were also detected in the chordwise plane and attributed to a Kelvin–Helmholtz instability (with a typical propagation velocity of $0.65 \cdot U_\infty$). A discussion of the origin of the buffet cells was also given in Ref. [16], where the buffet cells were described as reminiscent of the stall cells observed in low-speed conditions.

Reference [14] has also addressed the finite-wing effect, showing that for a finite swept wing, end effects and wall interference are present. These effects cause the formation of tip vortices, which influence the transonic buffet behavior in the more outboard sections [14] while recovering the infinite swept-wing behavior in the more inboard sections. These results are also confirmed by the numerical study of Ref. [17].

In contrast, finite-wing effects on transonic buffet in connection to unswept wings have received relatively little attention in the literature and require further research. Nevertheless, some studies have been conducted on the confinement effects on airfoils (therefore, in the absence of a free wingtip), such as in the numerical study of Ref. [18], where differences in the airfoil performance were noted when modeling top, bottom, and sidewalls of the wind tunnel. The authors of Ref. [3], by analyzing oil flow visualization results, commented that possible 3-D sidewall effects are contained in proximity of the two extremities of the airfoil model. However, there is not such a study in that literature that experimentally compares the performance of an airfoil and a finite unswept wing under transonic buffet conditions.

Besides the physical description given in Ref. [14], Ref. [19] has also described three-dimensional buffet by applying stability analysis to both swept and unswept infinite wings. In the presence of wing sweep, spatial modes were found to become unsteady, propagating periodic flow structures toward the wingtip, which is in good agreement with the existing literature. For an unswept wing, these spatial modes are still present, although steady, in addition to the classical 2-D buffet mode. This analysis has also been extended in Ref. [20] to finite wings.

It should be considered that the experimental swept-wing models investigated in the literature, as in the experimental database discussed in Ref. [9], differ from 2-D buffet models: not only for the presence of the sweep angle but also for the taper ratio and the presence of a fuselage. Therefore, it is difficult to isolate the effect of the sweep angle in transonic buffet. To achieve this goal in the current study, wings with different sweep angles and with constant chord have been studied and compared to the behavior of an airfoil that fully spans the wind-tunnel test section in order to quantify both sweep and tip effects.

Most of the experimental studies present in the literature make use of pressure measurements on the suction side of the wing, employing either unsteady pressure transducers [9,10,21] or pressure-sensitive paint [11,22,23]. In this paper, the main investigation is conducted by using stereoscopic particle image velocimetry (stereo-PIV) for reconstructing the three velocity components, in several planes of measurement oriented along the freestream direction, at different spanwise locations. The use of particle image velocimetry (PIV) is not uncommon in the study of transonic buffet on airfoils (see, for example, Refs. [5,24,25]); however, to the best of the authors' knowledge, no previous study has considered PIV to study transonic buffet on swept wings. The application of PIV could help to visualize and analyze the main flow structures characterizing transonic buffet on swept wings, which is not always allowed with wall pressure measurements.

In addition to PIV, the background-oriented schlieren (BOS) technique has been used to provide a further characterization of the flowfield. BOS was already successfully adopted in Ref. [6] for the study of transonic buffet on a 2-D airfoil, but its application in this intrinsically three-dimensional application has not been demonstrated yet and will be tested by comparing the results with PIV.

II. Experimental Investigation

A. Facility and Flow Conditions

The current experimental study has been performed in the transonic–supersonic wind tunnel (TST-27) of the Delft University of Technology, which is a blowdown wind tunnel with a test section that is 25.5 cm high and 28 cm wide. The experiments have been carried out with a total pressure of $p_0 = 2$ bars, a total temperature of $T_0 = 288$ K, and with the freestream Mach number in the range of $Ma_\infty = 0.70$–0.81 using a solid-wall test section with a boundary-layer thickness of 20 mm [26] and a freestream turbulence intensity of 3.5% [27]. The variation of the transonic Mach number is achieved by adjusting a throat located downstream of the test section, allowing an accuracy of Ma_∞ to the third decimal digit to be achieved. The values of the main flow conditions are reported in Table 1.

B. Wing Models

The models used for the experiments are wings obtained from the extrusion of an OAT15A airfoil with three different sweep angles of $\Lambda = 0$ deg, $\Lambda = 15$ deg, and $\Lambda = 30$ deg; a chord c of 8 cm; and a span b of 25 cm. The choice of the airfoil (OAT15A) and the values of the sweep angle are motivated by similar studies present in the literature (see Refs. [9,28]). The wings are clamped at the root to one of the sidewalls (see Fig. 1, right), with optical access provided from the opposite side of the test section. In addition to the three wings, an airfoil having a chord of 10 cm and a span of 28 cm (clamped at both sides of the wind tunnel) has been tested as well. This model has been extensively studied in the same wind tunnel for buffet applications in previous experiments [24]. For the finite-span wings, the distance of the wingtip to the side windows (3 cm) has been chosen to ensure that the wingtip was not immersed in the turbulent boundary layer developing on the sidewall of the test section.

A sketch of the top view of the different wing models is shown in Fig. 1 (left), with the main geometric characteristics included. In Fig. 1 (right), the 15 deg swept wing is shown together with the clamping piece by which the models are mounted to the wind-tunnel sidewall. Similar to other studies [3,5], a transition trip has been applied to all the models at 7% chord to ensure a turbulent boundary layer. The trip has been realized with Carborundum 500 (SiC) particles, as in Ref. [24].

Because the wing models are subject to higher loads in view of the different clamping conditions, high-performance Impax Supreme steel has been selected for the three wing models, whereas stainless steel has been used for the airfoil. Different natural frequencies of oscillation are thus obtained for the different models, as summarized in Table 2.

For the airfoil, the most developed buffet condition is obtained for $Ma = 0.7$ and $\alpha = 3.5$ deg, as shown in a previous experimental study [24] in the same wind tunnel. Correcting the Mach number for blockage effects, a value of $Ma = 0.73$ is achieved, which is in good agreement with the value found in Ref. [3] for the same airfoil.

The goal of this study is not that of evaluating and comparing the most developed buffet condition for the different models but rather to study the occurrence and the impact of finite-wing and sweep effects

Table 1 Flow conditions (normal with respect to leading edge)

Parameter	Symbol	Value
Freestream normal Mach number	$Ma_{\infty n}$	0.7
Freestream normal velocity	$U_{\infty n}$	225 m/s
Total temperature	T_0	288 K
Total pressure	p_0	2 bar
Reynolds number per unit length	Re/L	$2.6 \cdot 10^7$ 1/m

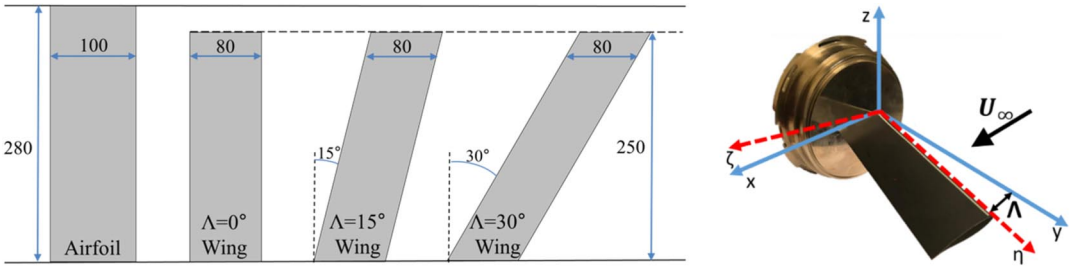

Fig. 1 Sketch of models based on OAT15A airfoil (left) with dimensions in millimeters and angles in degrees. On the right is the 15 deg sweep angle model attached to the clamping piece, with indication of the two coordinate systems used.

Table 2 Structural properties of the models

Parameter	Airfoil	Wings
Clamping conditions	Clamped–clamped	Clamped–free
Material	Stainless steel	Impax Supreme steel
Young modulus E, GPa	190	205
First natural frequency f_n, Hz	580	103

on transonic buffet while keeping all the other parameters constant. For this reason, in this study, the different wings are tested with the same value of the normal Mach number with respect to the leading edge ($Ma_{\infty n} = 0.7$), although the values of $Ma_{\infty n}$ and α for which the most developed buffet conditions are experienced may be different for the various models.

The values of the freestream Mach number and angle of attack used for each model are summarized in Table 3 together with the respective geometric parameters (chord and span).

C. Experimental Setup

The experiments have been conducted using two different optical techniques: background-oriented schlieren, and particle image velocimetry. BOS has been selected instead of schlieren because, for the three finite wings, the optical access was possible only from one side of the wind tunnel. The setup used for the BOS experiments consists of a light-emitting diode (LED) lamp for illumination and a high-speed recording camera looking directly at a speckle pattern, with the latter being attached to the clamping piece at the wing root. A sketch of the BOS setup in the top view is shown in Fig. 2 (left). A LaVision Imager Pro HS4 camera is used with an acquisition frequency of 4.65 kHz, which allows us to resolve the shock oscillation in time. To reach that acquisition frequency, the resolution of the camera has been cropped to 1008×468 pixels, acquiring 4000 images per wind-tunnel test. By using a 105 mm lens, a field of view (FOV) including the entire chord of the models has been obtained, as indicated in Fig. 2 (right).

Table 3 Flow and geometric properties of the models

Model	Ma_∞	α, deg	c, m	b, m
Airfoil	0.7	3.5	0.10	0.28
$\Lambda = 0$ deg wing	0.7	3.5	0.08	0.25
$\Lambda = 15$ deg wing	0.72	3.4	0.08	0.25
$\Lambda = 30$ deg wing	0.81	3.4	0.08	0.25

The speckle pattern has been realized with black dots on a white background. An example of the speckle pattern used is given for the unswept wing in Fig. 3 (left), with clear compressibility effects revealed in the area where the speckle pattern is deformed. The region in which high compressibility effects are evident is not a line, as it should be in the presence of a normal shock wave at a given spanwise position. The reason for this is associated with the integration of the variable-density gradient along the span of the wing/airfoil. To minimize the 3-D effects in the BOS images, the viewing direction of the camera has been aligned along the leading edge of the different wings, as is also sketched in Fig. 2 (left).

To quantitatively investigate the flowfield, stereo-PIV tests have been performed using the setup shown in Fig. 4 (left). Two high-speed cameras (Photron Fastcam SA1.1) in a stereoscopic configuration with an acquisition frequency of 4.65 kHz and in a double-pulse mode (pulse separation of $\Delta t = 3$ μs) have been used for acquiring images, for a total time duration of $t = 0.94$ s (4365 pairs of images per camera). To achieve the selected acquisition frequency, the sensor of the cameras has been cropped to 1024×640 pixels. Both cameras have been equipped with lenses with a focal length of 105 mm and an f stop of $f_\# = 8$; in addition, two Scheimpflug adaptors have been used to align the focal plane with the image plane (laser plane). These settings resulted in a field of view in the chordwise plane that is 8 cm long and 5 cm high (12 pixels/mm), as sketched in Fig. 2 (right). Limitations in the optical access have constrained the angle between the cameras to approximately 60 deg. The use of the stereoscopic configuration allows the determination of the out-of-plane velocity component, which is of crucial importance to characterize a 3-D flow.

The seeding particles used are diethylhexyl sebacates, which have a relaxation time of 2 μs (see Ref. [29]) and are produced by a PIVTEC GmbH PIVpart45 seeder with 45 Laskin nozzles. In view of their relaxation time, the particles are not able to faithfully follow the flow in regions of strong flow deceleration, as is notably occurring for shock waves. Therefore, in such flow regions, the velocity measurement is affected by a particle slip uncertainty ($\varepsilon_{\text{slip}} = 50$ m/s across the shock wave).

The particles are illuminated by a high-speed dual-cavity Mesa™ PIV laser (neodymium-doped yttrium aluminum garnet, Nd:YAG), forming a light sheet of 1.5 mm in thickness. The laser illumination was synchronized with the cameras using a LaVision high-speed

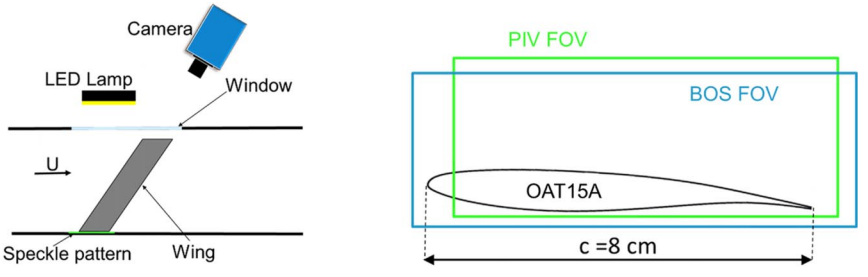

Fig. 2 Top view of BOS setup (left). On the right is the BOS and PIV FOVs.

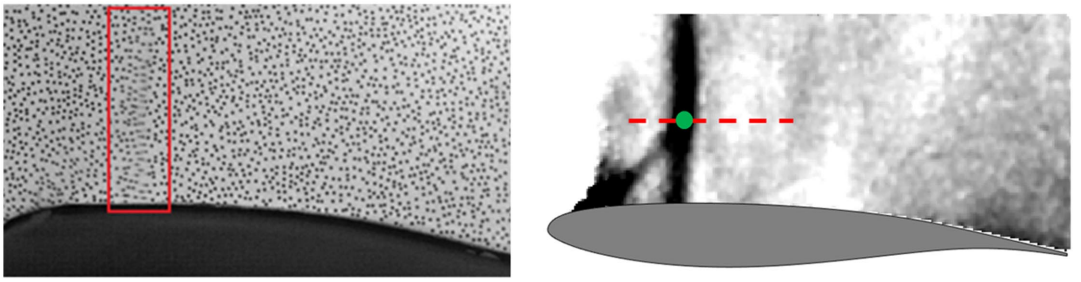

Fig. 3 Instantaneous image of the deformed speckle pattern (left) together with the processed BOS image, which displays the horizontal displacement of the speckle pattern (right).

controller (item-number 1108075). The laser beam is introduced in the test section by means of a laser probe entering from one of the sidewalls of the wind tunnel (see Fig. 4, left). By simultaneously sliding the laser probe and the cameras, tests at different span locations have been performed: in particular, at $y/b = 0.4$, 0.5, 0.6, and 0.7 for the unswept wing and at $y/b = 0.5$, 0.6, and 0.7 for the remaining two wings, as indicated in Fig. 4 (right).

D. Data Processing and Uncertainty

Both the BOS and the PIV images were collected and partly processed in LaVision Davis 10.0.5 software. For the BOS images, each instantaneous snapshot of the speckle pattern in the presence of density gradients was cross correlated with a reference image (obtained with the wind tunnel off). A multipass approach with an initial window size of 32×32 pixels, a final window size of 16×16 pixels, and an overlap of 75% was applied, reaching a final vector spacing of 0.028 cm (corresponding to 0.28% chord for the airfoil and 0.35% chord for the wings). In Fig. 3 (right), an example of a BOS processed image is shown, resulting from a cross correlation of the raw image in Fig. 3 (left) with the reference no-flow image. This processed image clearly quantifies the deformation of the pattern due to the (density) compressibility effects, and as such visualizes the near-normal shock wave as well as the oblique Mach wave originating from the transition trip.

For the PIV images, to reduce the laser reflections from the model, a minimum subtraction has been used by means of a Butterworth filter with a filter length of seven snapshots (for more details, see Ref. [30]). Subsequently, a stereoscopic cross-correlation procedure was performed, again using a multipass approach with an initial window size of 96×96 pixels, a final window size of 32×32 pixels, and an overlap of 75%. These settings resulted in a vector spacing of 0.82% chord. The vector uncertainty associated to the cross-correlation procedure can be computed similarly for BOS and PIV, as described in Ref. [31]. The associated value is lower than 0.1 pixels, and therefore leads to an uncertainty in the PIV velocity evaluation lower than 6.7 m/s. In Table 4, the main PIV and BOS settings as well as corresponding uncertainties are summarized (for a more detailed derivation of the PIV uncertainties, the reader is referred to Ref. [32]). Further processing for both BOS and PIV data has been carried out in MATLAB. To reduce the impact of the lack of vectors in the determination of the statistics, an outlier detection was carried out. A first detection of outliers was based on discarding vectors when their values were not included in ± 3 standard deviations with respect to the average value of both of the velocity components. Those outliers were substituted with an interpolation of the neighboring vectors. To correct images with large patches of outliers, caused by intermittent particle seeding, an interpolation in time instead of in space was applied as well.

Table 4 BOS and PIV settings and uncertainties

Parameter	BOS	PIV
Acquisition frequency, kHz	4.65	4.65
Number of images	4000	4365
Final image resolution, pixels	1008×468	1024×640
Final window size, pixels	16×16	32×32
Window overlap, %	75	75
Vector spacing, chord	0.28% (airfoil)–0.35% (wings)	0.82%
Cross-correlation uncertainty	<0.1 pixels	<6.7 m/s
Particle slip	Not applicable	<50 m/s (in shock areas)

III. Comparison of Airfoil and Unswept-Wing Behavior

A. Flow Features Analysis by Means of Oil Flow Visualizations

Although there are many studies in the literature that describe transonic buffet behavior on airfoils, there is no study where a comparison between the performance of an airfoil (clamped to both sides of the wind tunnel) and an equivalent unswept wing of finite span (with a free wingtip) is addressed. In this section, these two behaviors are directly compared using oil flow visualizations on two models at the same flow conditions ($Ma = 0.7$ and $\alpha = 3.5$ deg).

The main differences between the two oil flow visualizations (see Fig. 5) are in regard to the shock wave position and shape (red dashed lines), the separated area (blue solid line), and the tip effects. For the airfoil case, the shock wave appears relatively uniform along the span (except near the two extremities of the model due to sidewall influences) and is located around 40% chord. For the finite unswept wing, the shock wave position varies significantly along the span,

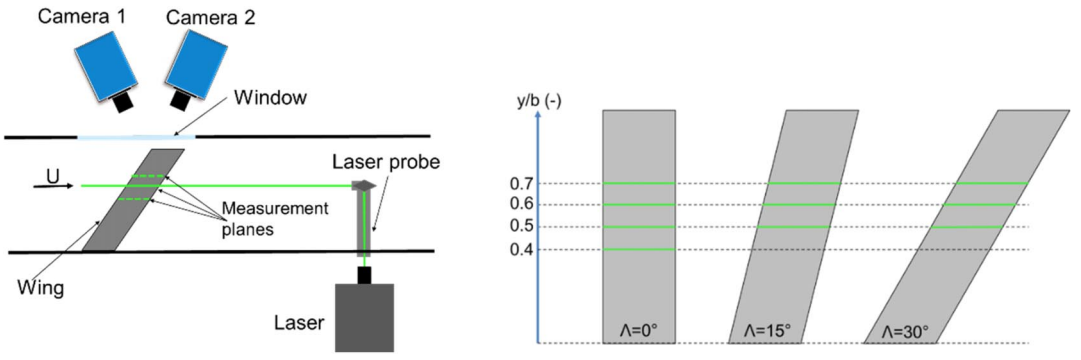

Fig. 4 Stereo-PIV setup (left) and location of the PIV planes of measurement (right).

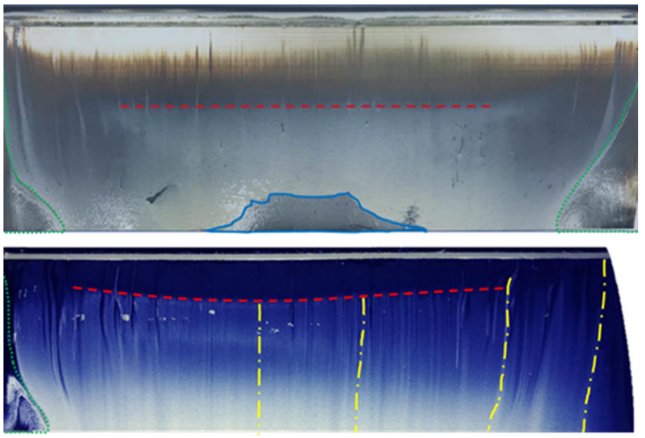

Fig. 5 Comparison of oil flow visualizations for airfoil (top) and unswept wing (bottom): average shock wave position (red dashed lines), separated area (blue solid line), corner effects (green dotted lines), and streamline orientation (yellow dashed lines).

with the most downstream shock wave position experienced in proximity of the midspan plane (slightly more inboard). It is also evident that for the unswept wing, the shock wave is located more upstream, with the average position at approximately 25% chord.

In correspondence with the clamping locations of the models (at both sides for the airfoil and at one side for the unswept wing), corner effects are highlighted with green dotted lines, with vortical structures indicating flow separation being present near the trailing edge of both the models tested. Moreover, for the unswept finite wing, a tip effect is also present, which results in an inboard flow contribution on the suction side of the model, in view of the pressure difference between the two sides of the model, which is in agreement with the literature (see, for example, Ref. [33]). As a result, the streamlines on the suction side of the unswept wing are clearly diverted inboard near the tip. Streamlines oriented along the freestream direction are only recovered at around $y/b = 0.5$ (see yellow dashed lines). It is worth pointing out that because the boundary-layer thickness on the sidewalls is about 20 mm [27] (whereas the distance of the wingtip to the sidewall is 30 mm), it is reasonable to assume that no interaction between the wingtip vortex and the sidewall boundary layer takes place.

Another important difference is the absence of a separated region for the unswept wing: at least in an average sense. Differently, this flow feature is clearly present for the airfoil, as underlined by the blue line in Fig. 5 (top).

B. Shock Dynamics Comparison by Means of BOS

Once a first qualitative visualization of the flowfield is given by means of oil flow visualizations, the shock position has been tracked for both configurations using the BOS images. In detail, the shock position has been tracked by evaluating the maximum of the gradient of the density field along horizontal lines, at $0.15c$ from the surface of the airfoil, as sketched in Fig. 3 (right).

The variation of the shock position in time is shown in Fig. 6 (left). As qualitatively observed from the oil flow visualizations, it is evident that the shock wave is located much more upstream for the unswept wing (the mean shock position for the unswept wing is $X_{\mathrm{SW\,AVG}} = 28.3\%$ of the chord; whereas for the airfoil, this is $X_{\mathrm{SW\,AVG}} = 42.8\%$ chord) and the amplitude of the oscillation is larger for the airfoil. This is confirmed by the standard deviation (STD) of the shock position, which is $X_{\mathrm{SW\,STD}} = 7.1\%$ chord for the airfoil and $X_{\mathrm{SW\,STD}} = 2.7\%$ chord for the unswept wing (these data are also summarized in Table 5). The values of the average shock position and STD reported for the airfoil are very similar to the values reported in Ref. [24] for the same flow conditions, as obtained with schlieren and PIV techniques, confirming the accuracy of BOS for 2-D applications.

When analyzing the shock position, it is evident that for the unswept-wing case, the shock behavior is less periodic, with higher-frequency contributions being observable in the shock wave behavior. To complete this discussion, the spectral content associated with the shock position for both the airfoil and the unswept wing is represented by its power spectral density (PSD) and shown in Fig. 6 (right). The PSD is computed with the Welch method, and each PSD is normalized by their respective variance. Both the configurations display a main contribution of the spectrum at about 160 Hz (like Ref. [24]). However, for the airfoil, a distinct peak is present at exactly 160 Hz; whereas for the unswept wing, there is a more broadband contribution with two relative peaks at 142 and 160 Hz. The general behavior of the PSD greatly differs for the two models, with the airfoil configuration having only minor contributions at frequencies other than 160 Hz, which is in contrast to the unswept wing. For the latter, additional contributions are present at 280–320 Hz, for which the frequency values are double the main buffet contributions (142–160 Hz). The reason for a higher energetic contribution at the first harmonic of the buffet frequency for the unswept wing is not certain. Nonetheless, it is supposed to be associated with a more irregular behavior of the shock wave position signal (also in view of the shock wave position variations along the span), which introduces contributions at the first harmonic of the buffet phenomenon. For the unswept wing, additional contributions associated with the structural vibration of the wing occur at 60 and 100 Hz. Although for frequencies above 1050 Hz there is a good agreement between the two PSDs, the frequency contributions between 500 and 1050 Hz are more relevant for the unswept wing. These frequencies correspond to Strouhal numbers of $St = 0.18$–0.4, which are in the same broadband range of Strouhal numbers that is often associated with the transonic buffet behavior of a swept wing [28]. This observation

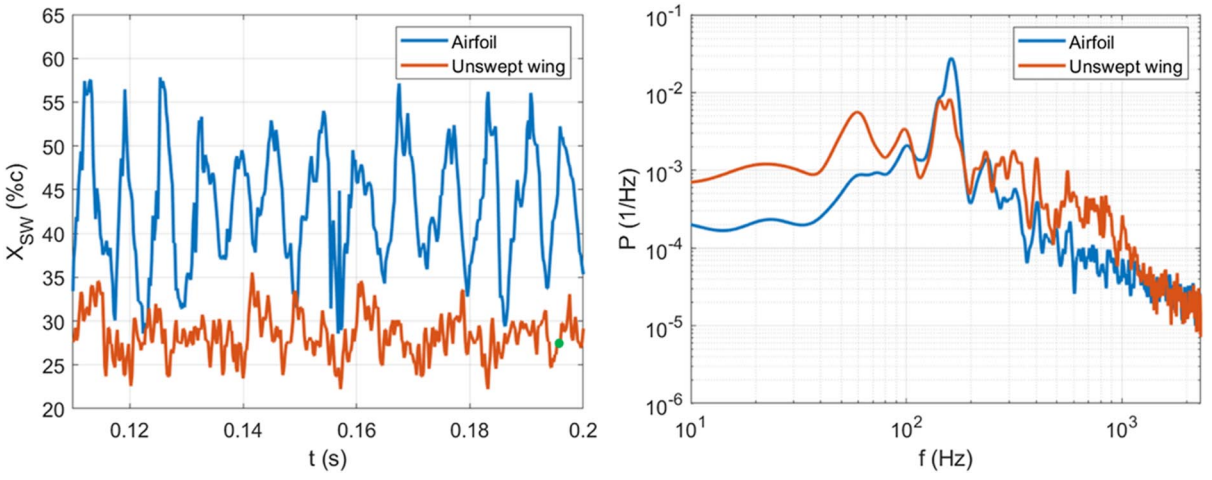

Fig. 6 Time behavior of shock position for airfoil and unswept wing (left) with relative power spectral density (right). The green dot in the left-side figure indicates the snapshot shown in Fig. 3.

Table 5 Average and standard deviation of shock wave position for different configurations

Configuration	SW_{AVG}, %c	SW_{STD}, %c
BOS, airfoil	42.8	7.1
BOS, $\Lambda = 0$ deg wing	28.3	2.7
PIV, $\Lambda = 0$ deg wing, $y/b = 0.4$	35.3	3.5
PIV, $\Lambda = 0$ deg wing, $y/b = 0.5$	35.2	3.3
PIV, $\Lambda = 0$ deg wing, $y/b = 0.6$	30.5	2.8
PIV, $\Lambda = 0$ deg wing, $y/b = 0.7$	27.7	2.4

suggests that the buffet phenomenon is highly influenced by finite-wing effects and clamping conditions.

C. Flowfield Analysis for the Unswept Wing

To better address the clamping condition effects, the PIV measurements carried out for the unswept wing at different spanwise positions ($y/b = 0.4$, 0.5, 0.6, and 0.7) are discussed. For this purpose, the average velocity field is shown in Fig. 7 (left) for the two most extreme measurement planes ($y/b = 0.4$ and $y/b = 0.7$). The comparison shows that in the most inboard section, the supersonic area encompasses a much wider region than for the plane of measurement in the neighborhood of the tip of the unswept wing. To better compare the average horizontal velocity fields, in Fig. 7 (right), the velocity profiles for $z/c = 0.2$ and for $0.1 < x/c < 0.95$ (corresponding to the dashed line in Fig. 7, left) are shown for all four measurement planes. The plot confirms an upstream shift of the average terminating shock position when moving from the most inboard test location to the most outboard. In addition, for the most outboard location, a further reduction of the velocity is observed for $0.5 < x/c < 0.95$. Very similar results are obtained for $y/b = 0.4$ and $y/b = 0.5$: both in terms of shock wave position and velocity development downstream of the shock wave.

These observations are in good agreement with an oil flow visualization performed on the same model and flow conditions (Fig. 5, bottom), where the most downstream shock wave position is observed within the range of $0.4 < y/b < 0.5$. In addition, the presence of both the wing root and wingtip interaction is noted.

The shock wave has been tracked using the PIV data by monitoring the gradient of the horizontal velocity component. The computed values of the average shock position and standard deviation are reported in Table 5. The results confirm the observations from Fig. 7, with more downstream shock wave positions being present for $y/b = 0.4$ and $y/b = 0.5$, where the widest range of oscillation of the shock wave is also achieved. By comparing the shock wave properties of the unswept wing computed with both BOS and PIV, it is evident that the BOS data are closer to the range of values observed for the most outboard PIV planes of measurement.

The power spectral densities associated with the shock wave position in the different measurement planes have been plotted in Fig. 8. The different spectra are practically overlapping over the entire spectrum, except for the most outboard location ($y/b = 0.7$). It is also interesting to note that for only the more outboard locations ($y/b = 0.6; 0.7$), the main buffet frequency contribution appears more broadband (as observed from the BOS data in Fig. 6, right); whereas at the more inboard locations, a distinct peak at 160 Hz is observed.

Comparing the spectral analysis in Fig. 8 (based on the PIV data) with the plot of Fig. 6 (right) (based on the BOS data), a very good match between the two techniques is achieved. This confirms that BOS is able to characterize the main features of buffet on an unswept wing, although it is not capable of characterizing the flow features at different spanwise locations.

IV. Effect of Sweep Angle

A. Instantaneous Flowfield

To describe the behavior of transonic buffet in the presence of the sweep angle, the instantaneous Mach number field (computed from the velocity data with the assumption of constant total temperature)

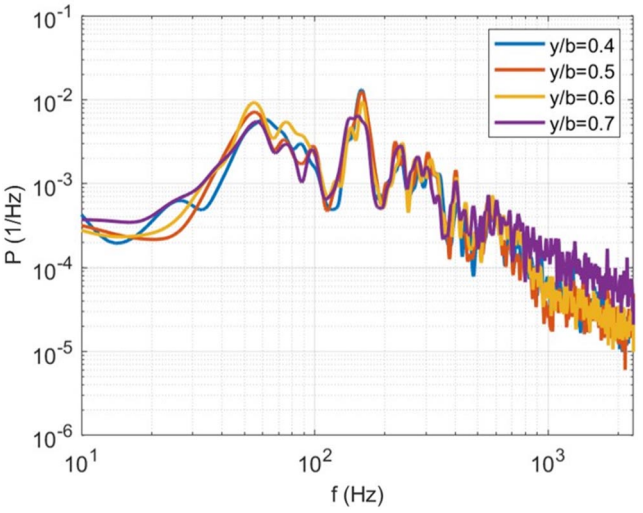

Fig. 8 Power spectral density of SW position tracked in the four different measurement planes from PIV measurements.

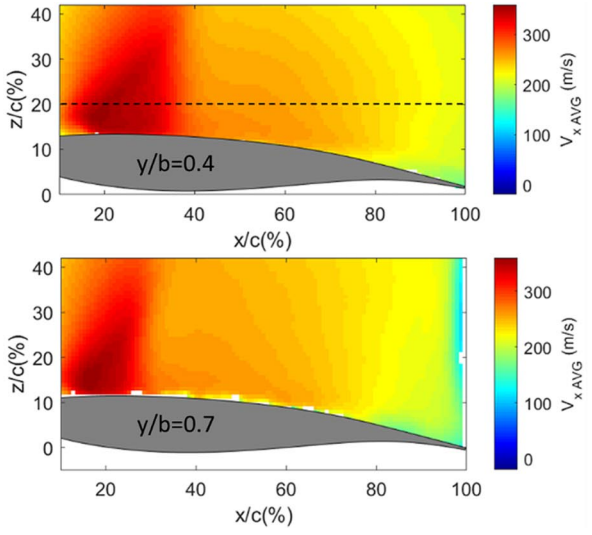

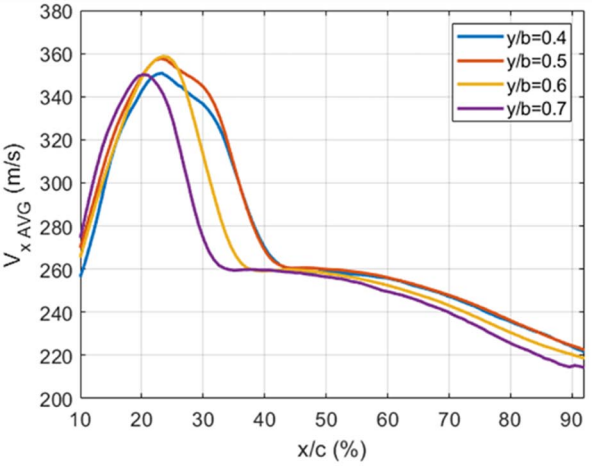

Fig. 7 Average streamwise velocity component V_x for $\Lambda = 0$ deg wing for $y/b = 0.4$ and $y/b = 0.7$ (left). On the right is the comparison of average velocity profiles for $z/c = 0.2$ and for $y/b = (0.4, 0.5, 0.6, 0.7)$.

is discussed for one entire buffet cycle for the $\Lambda = 30$ deg wing for $y/b = 0.6$. To analyze the cycle, six snapshots with a time separation of $3\Delta t$ (i.e., 0.645 ms; with $\Delta t = 0.215$ ms being the time interval between subsequent acquisitions) are taken into consideration (see Fig. 9).

In the first time step t_0, the shock wave is located in its most upstream position ($x/c = 0.35$). In the following image of Fig. 9 ($t = t_0 + 3\Delta t$), the shock wave moves downstream; and a region of accelerated flow is observed for $0.4 < x/c < 0.7$. In the following time step (image in the top right), this region has become locally supersonic; and a secondary shock wave structure appears at $x/c = 0.65$. In the figure in the bottom left, the main shock wave structure has moved downstream, whereas the secondary shock wave is moving upstream. As a result of the opposite motion of the two shock wave structures, they are observed to merge in the $t = t_0 + 12\Delta t$ image, with a primary shock wave structure reaching its most downstream position ($x/c = 0.5$). In the following time step, the shock wave again starts its upstream movement. A similar description of secondary supersonic areas can be found in Ref. [34] for a similar range of flow conditions (although for nonbuffet conditions) and is attributed to the curvature of the airfoil.

To characterize the time evolution of the Mach field for a larger interval, the profile of the Mach number field for $y/b = 0.6$ and $z/c = 0.2$ is shown in Fig. 10 for the $\Lambda = 15$ deg and the $\Lambda = 30$ deg wings. The Mach number profile of the latter (Fig. 10, right) clearly reveals the oscillation of the primary shock wave structure (between 40 and 55% chord) and the intermittent presence of a secondary supersonic area, which extends approximately until 80% chord. As shown from the instantaneous images in Fig. 9, the secondary supersonic area is formed during the second half of the downstream travel of the primary shock wave and disappears when this shock reaches its most downstream position.

Differently, the time evolution of the profile of the $\Lambda = 15$ deg wing (Fig. 10, left) shows a more upstream shock wave location (between 25 and 35% chord) with only subsonic expansions of the flow downstream of the supersonic area.

B. Averaged Velocity Fields

In Fig. 11, the time-averaged velocity fields for each of the three components (oriented along the x, y, and z axes, as defined in Fig. 1; right) is shown for the $\Lambda = 30$ deg swept wing for $y/b = 0.6$ (and with $Ma = 0.81$ and $\alpha = 3.4$ deg). The extent of the supersonic area is quite evident from both V_x (streamwise velocity component, in the direction of the wind-tunnel centerline) and V_y (velocity component along the y axis, in the direction normal to the wind-tunnel sidewall).

For this configuration, at least in an average sense, no appreciable separated area can be observed, with a relevant reduction of the streamwise velocity component occurring only in proximity of the trailing edge of the wing. The vertical velocity component (V_z, in the direction normal to the plane of the wing) has its maximum value in the most upstream region of the FOV, due to the curvature of the airfoil. A slight increase of vertical velocity is also observed in the shock wave oscillation area for $x/c \approx 0.45$. Regarding the out-of-plane velocity component V_y, in addition to the supersonic area, a region of negative velocity is observed in the area close to the trailing edge. In the

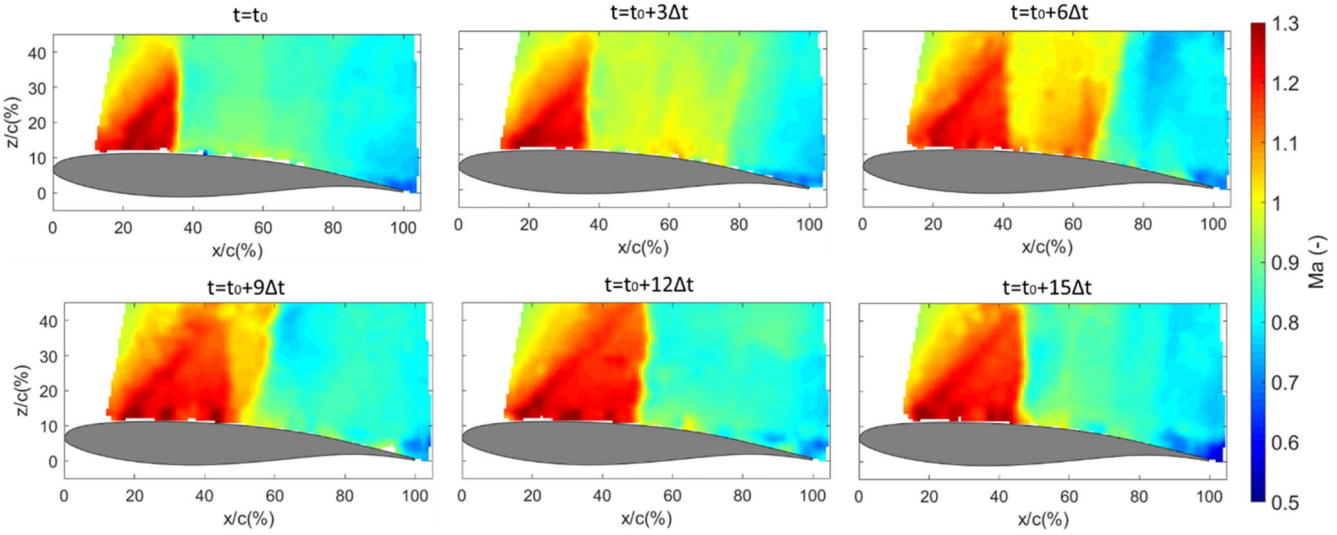

Fig. 9 Instantaneous visualization of the Mach number field in six different time steps for the $\Lambda = 30$ deg wing for $y/b = 0.6$.

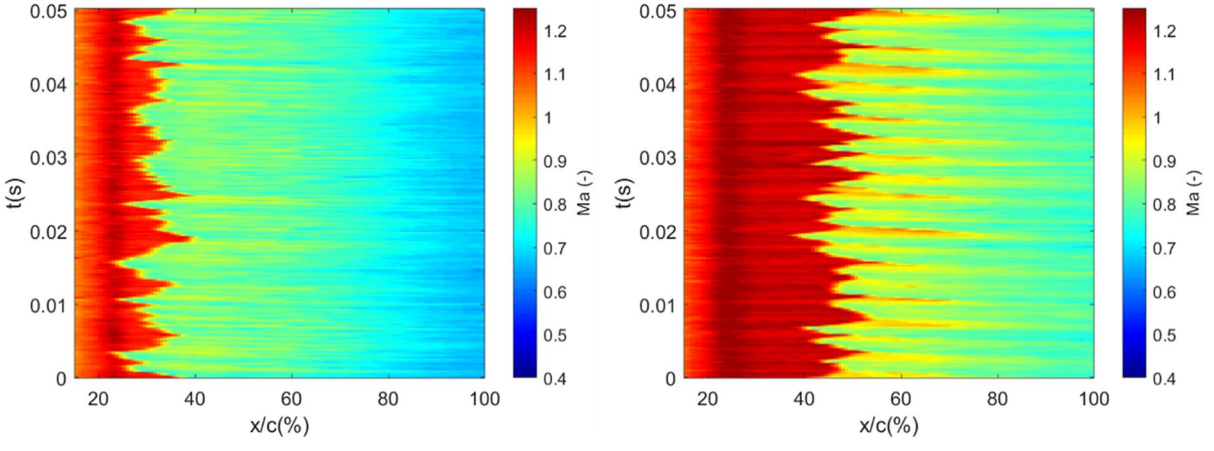

Fig. 10 Mach number profile for $y/b = 0.6$ and $z/c = 0.2$, for the $\Lambda = 15$ deg (left) and the $\Lambda = 30$ deg wings (right).

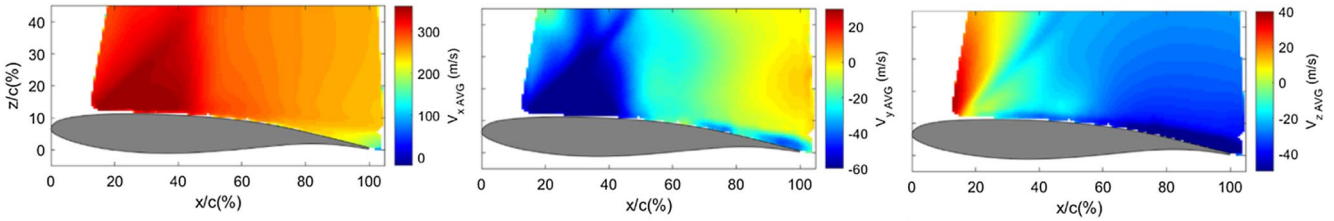

Fig. 11 Average velocity field for V_x (left), V_y (center), and V_z (right) for the 30 deg swept wing for $Ma = 0.81$ and $\alpha = 3.4$ deg at 60% of the span.

remaining portion of the FOV, the variations of velocity of the out-of-plane component remain limited.

To quantify the unsteadiness present in the velocity field, the standard deviations of the three velocity components are shown in Fig. 12 for the same plane of measurement ($y/b = 0.6$). The plot clearly shows unsteadiness due to the shock oscillation for both the streamwise (left) and the out-of-plane velocity components (center) in the range $0.4 < x/c < 0.5$. Although upstream of the shock wave the unsteadiness is very limited, additional unsteadiness (caused by the pulsating formation of the secondary supersonic region) is observed downstream ($0.5 < x/c < 0.6$). Further fluctuations occur, for all the velocity components, in proximity of the trailing edge, suggesting the presence of an intermittent separated area. For the vertical velocity component (right), relevant oscillations are observed between 40 and 60% of the chord and are attributed to fluctuations of the shock wave position and inclination throughout the buffet cycle.

For brevity, for the 15 deg sweep angle wing, only the horizontal velocity component and the corresponding standard deviation are presented (see Fig. 13). It is clear that, compared to the 30 deg wing, the extent of the supersonic area is much more limited, with the shock wave located more upstream ($x/c \approx 0.3$) and the relative amplitude of oscillation reduced to 10% chord. No unsteadiness is present at the trailing edge of the wing, suggesting that for this configuration and these flow conditions, the separated area is not even present in an intermittent fashion. No velocity fluctuations are observed downstream of the shock wave oscillation range, confirming the absence of a secondary supersonic area.

C. Shock Dynamics

To quantitatively compare the behavior of the shock wave for the different configurations, its position has been tracked in all the PIV measurement planes, as commented on previously for the unswept wing in Sec. III.

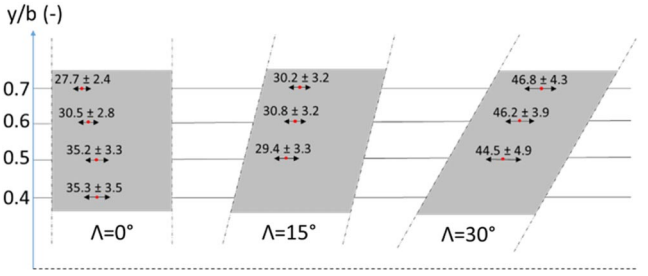

Fig. 14 Sketch of the three wings with indication of average and standard deviation of shock wave oscillation for each plane of measurement.

In Fig. 14, the region of oscillation of the shock position is indicated for all the wings and for all the span locations, providing its average value and the relative standard deviation. The wing with the largest amplitude of oscillation is the $\Lambda = 30$ deg wing, for which the values of the STD are in the range of 3.9–4.9% chord. From the BOS images, a slight underestimation of the fluctuations of the shock position is obtained for the $\Lambda = 30$ deg wing, with $SW_{STD\text{-}BOS} = 3.8\%$ chord. The PIV data confirm that in presence of the largest sweep angle, the most downstream average shock wave positions are achieved ($0.44 < X_{SW\,Avg}/c < 0.47$). In contrast, for both $\Lambda = 0$ deg and $\Lambda = 15$ deg, values close to 30% chord are computed. However, it should be remembered that, although the normal Mach number is constant, the freestream Mach number differs for each of the wings. From the comparison of the range of the shock wave oscillations, it emerges that only for the unswept wing is there a relevant variation of the shock wave position along the span. This observation may be explained by the fact that in presence of sweep angle, the tip vortex affects a smaller extent of the span.

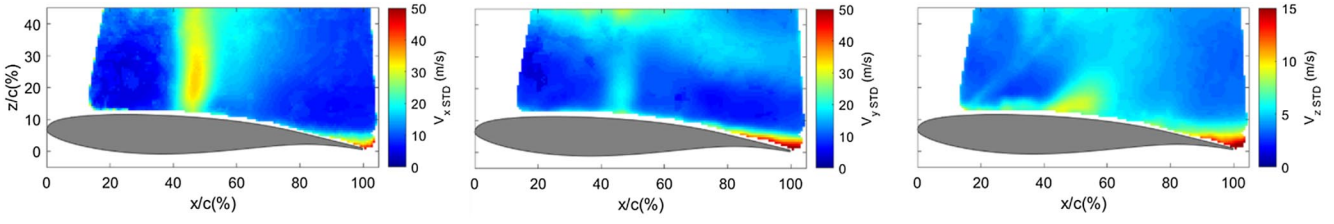

Fig. 12 Standard deviation of velocity field for V_x (left), V_y (center), and V_z (right) for the 30 deg swept wing for $Ma = 0.81$ and $\alpha = 3.4$ deg at 60% of the span.

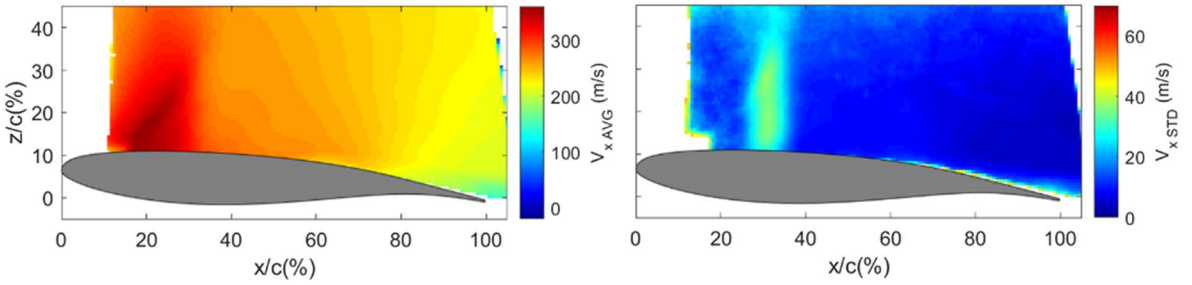

Fig. 13 Average (left) and standard deviation (right) of velocity field for the V_x component of the 15 deg swept wing for $Ma = 0.72$ and $\alpha = 3.4$ deg at 60% of the span.

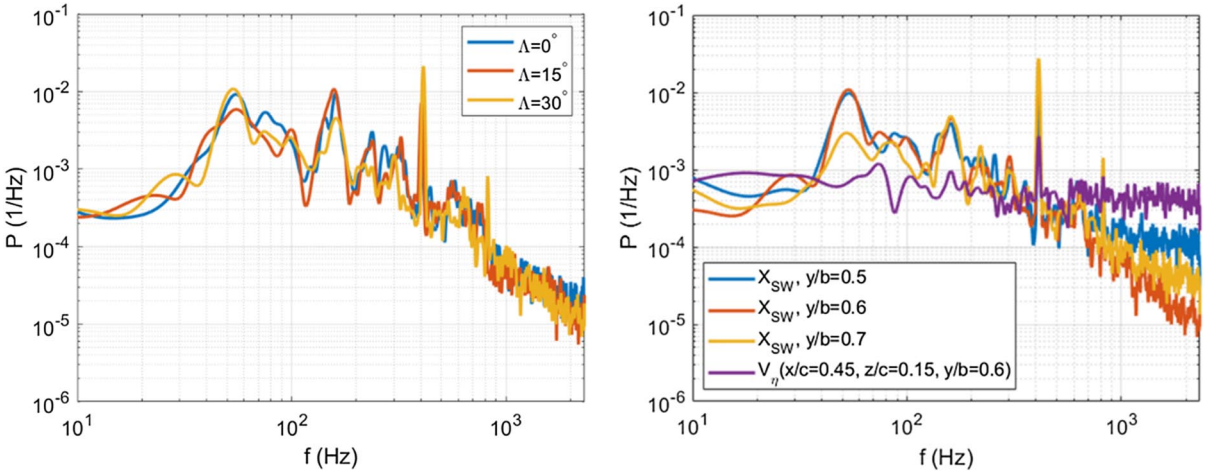

Fig. 15 Comparison of PSD of SW position for different wings for $y/b = 0.6$ (left). The right shows comparison of PSD of SW position for different measurement planes ($y/b = 0.5, 0.6, 0.7$) for $\Lambda = 30$ deg wing. Purple line indicates PSD of spanwise velocity component in $x/c = 0.45$, $z/c = 0.15$, and $y/b = 0.6$.

From the time behavior of the shock position, the corresponding power spectral density has been determined for all the measurement planes. To have a comparison between the spectral content of the shock wave position for the different wings, the PSD of the shock position is shown for all the wings and for the same spanwise plane of $y/b = 0.6$ in Fig. 15 (left). The wings exhibit a similar spectral content, with main contributions at 60 Hz (oscillation of the model), 160 Hz (2-D buffet frequency), and 400 Hz (wind-tunnel contribution). In addition to these peaks, additional energetic contributions are observed in the range of 450–850 Hz that, as previously commented, is in the same range of frequencies obtained in the literature for 3-D buffet. When comparing the different configurations, it is also observed that, with the increasing value of the sweep angle (also associated with an increase of the freestream Mach number), there is an increase in the wind-tunnel contribution at 400 Hz.

To verify variations in the spectral content of the shock wave oscillation along the span, the PSDs of the shock wave position are compared for the different measurement planes of the 30 deg sweep angle wing (see Fig. 15, right). Also, in this case, a similar distribution of the PSDs is observed, with no variation in the relevance of the 2-D buffet peak (at 160 Hz) or in the range of 450–850 Hz. However, an increase of the values of the PSDs for $f > 1000$ Hz is observed for both $y/b = 0.7$ and $y/b = 0.5$ as compared to $y/b = 0.6$.

D. Spanwise Velocity Component

To analyze the spanwise behavior of the velocity field, a rotated coordinate system oriented along the leading edge of the wings η and in the orthogonal direction ζ has been adopted (see the two coordinate systems in Fig. 1, right). The velocity component orthogonal to the leading edge V_ζ and the one oriented along the leading-edge direction of the wing V_η are computed as

$$V_\zeta = V_x \cos\Lambda - V_y \sin\Lambda \tag{1}$$

$$V_\eta = V_x \sin\Lambda + V_y \cos\Lambda \tag{2}$$

with V_η being positive, going from the root to the tip of the wing. In Fig. 16, the average spanwise velocity is shown for the $\Lambda = 30$ deg wing for all the measurement planes ($y/b = 0.5$ on the left, $y/b = 0.6$ in the center, and $y/b = 0.7$ on the right). In the large part of the FOV, there is a nearly uniform outboard velocity of approximately 120 m/s in the shock wave oscillation region and in the range from 70 to 100 m/s in the trailing-edge area.

The values of the spanwise component in the trailing-edge area are very close to the convection velocity obtained by Ref. [10] for the buffet cells. Differently, the value of spanwise velocity in the shock wave oscillation range is higher than the convection velocity obtained by Refs. [9,10] (where a convection velocity of approximately 60 m/s was reported).

In Fig. 15 (right), the spectral content of the time variation of the spanwise velocity component V_η in a point in the shock wave oscillation range is reported ($x/c = 0.45$, $z/c = 0.1$, and $y/b = 0.6$). No relevant contributions are observable at the 2-D buffet frequency (160 Hz), whereas relative higher energetic contributions are present at higher frequencies.

V. Conclusions

In this paper, transonic buffet has been studied experimentally to investigate finite-wing and sweep effects. This study showed an appreciable difference in the transonic buffet behavior between a full-span unswept wing (airfoil) and an unswept wing of finite span (clamped on just one side of the wind tunnel). The results clearly reveal that the buffet oscillations are more relevant and periodic in the case of the airfoil than for the unswept wing (see Fig. 6), with the shock wave located much more downstream in the former case. The use of PIV in different planes of measurement demonstrated that the shock wave is located more upstream and oscillating in a more restricted region at outboard locations (Fig. 7). These results suggest that at those locations, an effect of the wingtip vortex on the buffet behavior is felt, as was also supported by additional oil flow visualization. Spectral analysis showed that the presence of the free tip of the wing also gives rise to structural oscillation of the wing.

The application of both BOS and PIV for the study of the unswept wing has also validated the use of the BOS technique for analyzing transonic buffet on models with 3-D structures developing along the

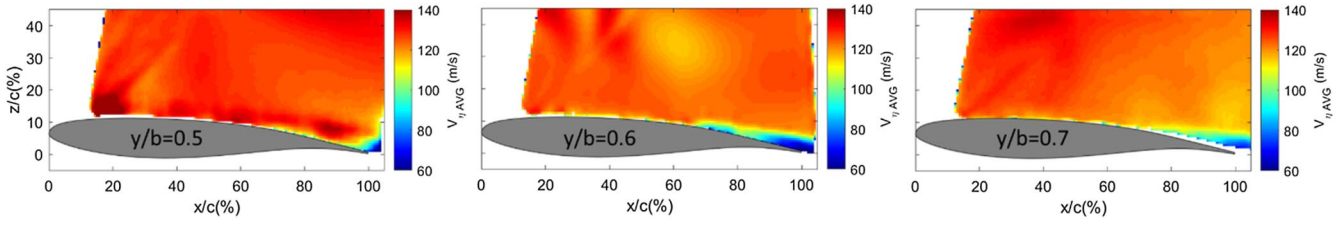

Fig. 16 Comparison of spanwise component of velocity for the $\Lambda = 30$ deg wing for $y/b = 0.5$ (left), $y/b = 0.6$ (center), and $y/b = 0.7$ (right).

span. From the BOS images, it has been possible to obtain results in agreement with the PIV data: in particular, in terms of the amplitude of the shock wave oscillation. Thus, the use of the BOS technique could be applied to future studies of transonic buffet on unswept wings, especially when a qualitative visualization of the flowfield is needed, or for the identification of the most developed buffet conditions, for which purpose obtaining PIV measurements could be too time consuming. Additional discrepancies could arise from BOS measurements on swept models in view of the additional spanwise variability of the flowfield. Notwithstanding this, by orienting the BOS camera in the direction of the leading edge of the wings, a good approximation (although underestimated) of the amplitude of the shock wave is obtained.

To analyze the effect of the sweep angle, the behaviors of wings with different sweep angles ($\Lambda = 0$, 15, and 30 deg) have been compared, using the same normal Mach number for each wing (with respect to the wing leading edge). At these flow conditions, much more downstream shock wave positions and a wider range of oscillations are achieved for the $\Lambda = 30$ deg wing, whereas similar results are observed for the other two wings (see Fig. 14). For the configuration with the larger sweep angle, a periodic formation of a secondary supersonic area characterizes the shock wave oscillations during the buffet cycle. An analogous behavior was not observed for the $\Lambda = 15$ deg and the unswept wings (Fig. 10).

Evidence was found of an intermittent separated trailing-edge area that occurs only for the larger sweep angle wing (Figs. 11 and 12). Near the trailing-edge region of the $\Lambda = 30$ deg wing, spanwise velocity components are found that are in the same range of the convection velocities obtained by Refs. [9,10] for the buffet cells. To better visualize the buffet cells, a PIV analysis in a measurement plane oriented along the span or with a volumetric setup (tomographic PIV) is suggested for further studies.

A similar frequency content of the shock wave dynamics has been observed for the three wings. For all the models, there is a reduction of the 2-D buffet peak as compared to the airfoil case, together with an increase for frequencies in the range of 450–850 Hz. Regarding the primary buffet frequency, a reduced relevance of the peak at 160 Hz has been noticed for the $\Lambda = 30$ deg as compared to the other wings. No relevant variations are instead visualized along the span of the swept wing. The increase of frequency contributions in the range between 450 and 850 Hz agrees with literature in terms of the Strouhal number ($St = 0.18$–0.4).

Although these results show some variations in the shock wave buffet oscillation in the presence of an increasing sweep angle, the current findings also indicate that an aspect that could influence the comparison of the behavior of an airfoil and that of a wing is the different mechanical boundary conditions associated with the clamping of the model, which lead to different structural oscillations and to the occurrence of tip effects for the wings. These differences introduce a nonsymmetric spanwise flow distribution for the unswept wing with respect to the airfoil (see Fig. 5). Therefore, it is suggested for future research that the buffet behavior of a finite-span swept wing is also compared with the corresponding unswept (finite-span) wing in addition to the corresponding airfoil. Similarly, the effect of the boundary conditions of an unswept-wing model in transonic buffet conditions should be further studied to better visualize and investigate the effect of wingtip vortices.

Acknowledgments

This work has been carried out as part of the Holistic Optical Metrology for Aero-Elastic Research project, funded by the European Commission's H2020 program under grant no. 769237. The authors acknowledge Carlos Camps Pons for having helped in conducting the experiments.

References

[1] Hilton, W. F., and Fowler, R. G., "Photographs of Shock Wave Movement," NPL R&M 2692, National Physical Laboratories, U.K., 1947.

[2] Lee, B. H. K., "Transonic Buffet on a Supercritical Aerofoil," *Aeronautical Journal*, Vol. 94, No. 935, 1990, pp. 143–152. https://doi.org/10.1017/S0001924000022752

[3] Jacquin, L., Molton, P., Deck, S., Maury, B., and Soulevant, D., "Experimental Study of Shock Oscillation Over a Transonic Supercritical Profile," *AIAA Journal*, Vol. 47, No. 9, 2009, pp. 1985–1994. https://doi.org/10.2514/1.30190

[4] Garnier, E., and Deck, S., "Large-Eddy Simulation of Transonic Buffet over a Supercritical Airfoil," *Direct and Large-Eddy Simulation VII*, edited by V. Armenio, B. Geurts, and J. Fröhlich, Springer, Dordrecht, The Netherlands, 2010, pp. 549–554. https://doi.org/10.1007/978-90-481-3652-0_81

[5] Hartmann, A., Feldhusen, A., and Schröder, W., "On the Interaction of Shock Waves and Sound Waves in Transonic Buffet Flow," *Physics of Fluids*, Vol. 25, No. 2, 2013, Paper 026101. https://doi.org/10.1063/1.4791603

[6] D'Aguanno, A., Schrijer, F. F. J., and van Oudheusden, B. W., "Spanwise Organization of Upstream Traveling Waves in Transonic Buffet," *Physics of Fluids*, Vol. 33, July 2021, Paper 106105. https://doi.org/10.1063/5.0062729

[7] Crouch, J. D., Garbaruk, A., Magidov, D., and Travin, A., "Origin of Transonic Buffet on Aerofoils," *Journal of Fluid Mechanics*, Vol. 628, March 2009, pp. 357–369. https://doi.org/10.1017/S0022112009006673

[8] Sartor, F., Mettot, C., and Sipp, D., "Stability, Receptivity, and Sensitivity Analyses of Buffeting Transonic Flow over a Profile," *AIAA Journal*, Vol. 53, Jan. 2015, pp. 1980–1993. https://doi.org/10.2514/1.J053588

[9] Paladini, E., Dandois, J., Sipp, D., and Robinet, J., "Analysis and Comparison of Transonic Buffet Phenomenon over Several Three-Dimensional Wings," *AIAA Journal*, Vol. 57, Nos. 1–18, 2018, pp. 379–396. https://doi.org/10.2514/1.J056473

[10] Dandois, J., "Experimental Study of Transonic Buffet Phenomenon on a 3D Swept Wing," *Physics of Fluids*, Vol. 28, June 2016, Paper 016101. https://doi.org/10.1063/1.4937426

[11] Sugioka, Y., Numata, D., Asai, K., Koike, S., Nakakita, K., and Koga, S., "Unsteady PSP Measurement of Transonic Buffet on a Wing," *53rd AIAA Aerospace Sciences Meeting*, AIAA Paper 2015-0025, Jan. 2015.

[12] Ohmichi, Y., Ishida, T., and Hashimoto, A., "Modal Decomposition Analysis of Three-Dimensional Transonic Buffet Phenomenon on a Swept Wing," *AIAA Journal*, Vol. 56, No. 10, 2018, pp. 3938–3950. https://doi.org/10.2514/1.J056855

[13] Mayer, R., Lutz, T., Krämer, E., and Dandois, J., "Control of Transonic Buffet by Shock Control Bumps on Wing-Body Configuration," *Journal of Aircraft*, Vol. 56, Oct. 2019, pp. 556–568. https://doi.org/10.2514/1.C034969

[14] Iovnovich, M., and Raveh, D. E., "Numerical Study of Shock Buffet on Three-Dimensional Wings," *AIAA Journal*, Vol. 53, Jan. 2015, pp. 449–463. https://doi.org/10.2514/1.J053201

[15] Roos, F. W., "The Buffeting Pressure Field of a High-Aspect-Ratio Swept Wing," *18th Fluid Dynamics and Plasma Dynamics and Lasers Conference*, AIAA Paper 1985-1609, July 1985.

[16] Plante, F., Dandois, J., and Laurendeau, E., "Similarities Between Cellular Patterns Occurring in Transonic Buffet and Subsonic Stall," *AIAA Journal*, Vol. 58, No. 1, 2019, pp. 71–84. https://doi.org/10.2514/1.J058555

[17] Plante, F., Dandois, J., Sartor, F., and Laurendeau, E., "Study of Three-Dimensional Transonic Buffet on Swept Wings," *35th AIAA Applied Aerodynamics Conference*, AIAA Paper 2017-3903, June 2017.

[18] Thiery, M., and Coustols, E., "Numerical Prediction of Shock Induced Oscillations over a 2-D Airfoil: Influence of Turbulence Modelling and Test Section Walls," *International Journal of Heat and Fluid Flow*, Vol. 27, No. 4, 2006, pp. 661–670. https://doi.org/10.1016/j.ijheatfluidflow.2006.02.013

[19] Crouch, J., Garbaruk, A., and Strelets, M., "Global Instability in the Onset of Transonic-Wing Buffet," *Journal of Fluid Mechanics*, Vol. 881, July 2019, pp. 3–22. https://doi.org/10.1017/jfm.2019.748

[20] Timme, S., "Global Instability of Wing Shock-Buffet Onset," *Journal of Fluid Mechanics*, Vol. 885, Jan. 2020, pp. 1–21. https://doi.org/10.1017/jfm.2019.1001

[21] Koike, S., Ueno, M., Nakakita, K., and Hashimoto, A., "Unsteady Pressure Measurement of Transonic Buffet on NASA Common Research Model," AIAA Paper 2016-4044, 2016. https://doi.org/10.2514/6.2016-4044

[22] Masini, L., Timme, S., and Peace, A. J., "Analysis of a Civil Aircraft Wing Transonic Shock Buffet Experiment," *Journal of Fluid*

Mechanics, Vol. 884, Dec. 2019, pp. 1–15.
https://doi.org/10.1017/jfm.2019.906

[23] Lawson, S. G., Greenwell, D., and Quinn, M., "Characterisation of Buffet on a Civil Aircraft Wing," *54th AIAA Aerospace Science Meeting*, AIAA Paper 2016-1309, Jan. 2016.

[24] D'Aguanno, A., Schrijer, F. F. J., and van Oudheusden, B. W., "Experimental Investigation of the Transonic Buffet Cycle on a Supercritical Airfoil," *Experiments in Fluids*, Vol. 62, May 2021, Paper 214.
https://doi.org/10.1007/s00348-021-03319-z

[25] Feldhusen-Hoffmann, A., Lagemann, C., Loosen, S., Meysonnat, P., Klaas, M., and Schröder, W., "Analysis of Transonic Buffet Using Dynamic Mode Decomposition," *Experiments in Fluids*, Vol. 62, April 2021, Paper 66.
https://doi.org/10.1007/s00348-020-03111-5

[26] Humble, R., Elsinga, G., Scarano, F., and van Oudheusden, B. W., "Three-Dimensional Instantaneous Structure of a Shock Wave/Turbulent Boundary Layer Interaction," *Journal of Fluid Mechanics*, Vol. 622, Feb. 2009, pp. 33–62.
https://doi.org/10.1017/S0022112008005090

[27] Tambe, S., "Boundary-Layer Instability on Rotating Cones," Ph.D. Thesis, Delft Univ. of Technology, Delft, The Netherlands, 2022.

[28] Giannelis, N. F., Vio, G. A., and Levinski, O., "A Review of Recent Developments in the Understanding of Transonic Shock Buffet," *Progress in Aerospace Sciences*, Vol. 92, March 2017, pp. 39–84.
https://doi.org/10.1016/j.paerosci.2017.05.004

[29] Ragni, D., Schrijer, F. F. J., van Oudheusden, B. W., and Scarano, F., "Particle Tracer Response Across Shocks Measured by PIV," *Experiments in Fluids*, Vol. 50, Oct. 2011, pp. 53–64.
https://doi.org/10.1007/s00348-010-0892-2

[30] Sciacchitano, A., and Scarano, F., "Elimination of PIV Light Reflections via a Temporal High Pass Filter," *Measurement Science and Technology*, Vol. 25, No. 8, 2014, Paper 084009.
https://doi.org/10.1088/0957-0233/25/8/084009

[31] Rajendran, L., Zhang, J., Bhattacharya, S., Bane, S., and Vlachos, P., "Uncertainty Quantification in Density Estimation from Background Oriented Schlieren (BOS) Measurements," *Measurement Science and Technology*, Vol. 31, No. 5, 2019, Paper 054002.
https://doi.org/10.1088/1361-6501/ab60c8

[32] Sun, Z., "Micro Ramps in Supersonic Turbulent Boundary Layers," Ph.D. Thesis, Delft Univ. of Technology, Delft, The Netherlands, 2014.

[33] Petrilli, J. L., Paul, R. C., Gopalarathnam, A., and Frink, N. T., "A CFD Database for Airfoils and Wings at Post-Stall Angles of Attack," *31st AIAA Applied Aerodynamics Conference*, AIAA Paper 2013-2916, June 2013.

[34] Kuzmin, A., "On the Lambda-Shock Formation on ONERA M6 Wing," *International Journal of Applied Engineering Research*, Vol. 9, No. 20, 2014, pp. 7029–7038.

D. E. Raveh
Associate Editor